

Insights into the Nature of Formate Species in the Decomposition and Reaction of Methanol over Cerium Oxide Surfaces: A Combined Infrared Spectroscopy and Density Functional Theory Study

P. G. Lustemberg,[†] M. V. Bosco,[‡] A. Bonivardi,^{*,‡,§} H. F. Busnengo,^{*,†} and M. V. Ganduglia-Pirovano^{||}

[†]Instituto de Física Rosario, CONICET-UNR, and Facultad de Ciencias Exactas, Ingeniería y Agrimensura, UNR, 2000 Rosario, Argentina

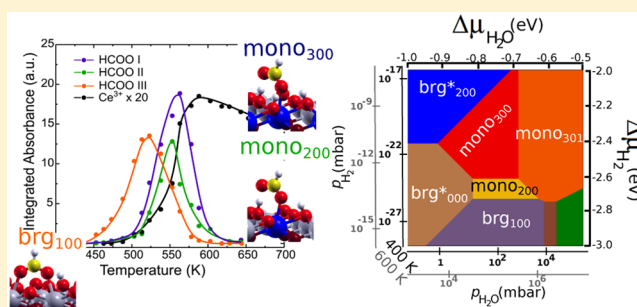
[‡]Instituto de Desarrollo Tecnológico para la Industria Química, UNL-CONICET, 3000 Santa Fe, Argentina

[§]Facultad de Ingeniería Química, UNL, 3000 Santa Fe, Argentina

^{||}Instituto de Catálisis y Petroleoquímica (ICP-CSIC), Madrid E-28049, Spain

Supporting Information

ABSTRACT: Formation of formate species on oxide surfaces plays a role in reactions for hydrogen production such as the water–gas shift and the steam-reforming of alcohols. It has been suggested that bridge formates are the most common and stable configuration on metal oxides. Ceria-based catalysts are important for these reactions where ceria is a “non-innocent” support. In this work, the nature of the formate species that are formed during decomposition and reaction of methanol on ceria surfaces have been studied using a combination of infrared temperature-programmed surface reaction (TPSR-IR) on a real powder catalyst support and density functional theory (DFT) together with statistical thermodynamics for model CeO₂(111) surfaces. The influence of surface oxygen vacancies, hydroxyl groups, and water has been considered. Three different formate species have been identified (450–550 K). Initially, formates are adsorbed on the oxidized surface that is gradually hydroxylated by the release of hydrogen from methoxy groups (>500 K), which leads to a partially reduced surface. On the former, one kind of species is observed, whereas on the latter, the other two kinds appeared. We provide computational evidence that the bonding is only initially of the bridge type but becomes of the monodentate type as the surface concentration of hydroxyl groups rises. The calculated frequencies of the O–C–O symmetric and asymmetric stretching modes for the three structures are in good agreement with those experimentally observed. The existence of monodentate species is discussed in terms of a stabilizing effect of hydrogen bonds. The combined experimental and theoretical results on real and model systems, respectively, thus provide important insights on the reaction of methanol on ceria surfaces.



1. INTRODUCTION

Ceria-based materials have a wide variety of applications including gas sensors, solid-state electrolytes, and automotive exhaust catalysts among others.^{1–8} In particular, ceria is used in heterogeneous catalysis as support or promoter to improve the activity, selectivity, and/or stability of the catalysts. One of the key properties of ceria is its oxygen storage capacity, which originates in its ability to rapidly switch from Ce³⁺ to Ce⁴⁺ oxidation states as the environment changes from reducing to oxidizing and vice versa. This property makes ceria-based materials indispensable for the conversion of pollutants to environmentally acceptable products in exhaust catalysis. Moreover, the active role of ceria in the important water–gas shift (WGS, CO + H₂O → CO₂ + H₂) and steam-reforming of alcohols reactions for hydrogen production, in particular the methanol steam-reforming reaction (MSR, CH₃OH + H₂O → CO₂ + 3 H₂), has been widely reported.^{9–17}

The possibility of understanding the mechanism of catalytic reactions, which is essential for rational catalyst design, depends very much on the chances of isolating intermediates in the study of each step in the catalytic cycle. It has been argued that formate (HCOO) transient species might be playing intermediate or spectator roles during WGS^{18–23} and MSR²⁴ or its reverse reaction,^{25–28} that is, methanol synthesis from carbon oxides.

Formates have been identified by different spectroscopic techniques. In particular, IR spectroscopy has been used to discriminate various kinds of formate species.^{29–31} Yet, the assignment of particular features in IR spectra to a chemisorbed species is in general not trivial: Strong bonding to the surface significantly affects the vibrational frequencies, and the different

Received: May 28, 2015

Revised: August 15, 2015

Published: August 17, 2015

ways in which species anchor to the surface result in complex IR spectra because of the possible distinct vibrations of each species.

According to their coordination to the surface, chemisorbed formates are often classified as monodentate, bidentate, and bridge species (Figure 1). A monodentate formate is one that is

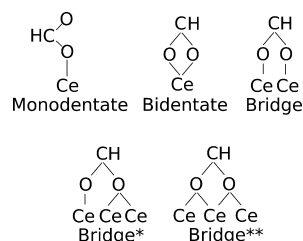


Figure 1. Schematic structures of surface formates considered in this work.

bonded to one surface metal atom through an oxygen atom. Formates with both oxygen atoms bound to the same surface metal atom are usually referred to as bidentate, whereas those formates bound to two or more metal atoms can be called bridge.

Busca and Lorenzelli made an important effort to classify diverse coordination geometries of formates upon scrutiny of IR spectra recorded for several oxides.³² Formate structures with different coordination are usually identified by measuring the frequency shift between the asymmetric and the symmetric O–C–O stretching mode, $\Delta\nu = \nu_{\text{OCO}}^{\text{asym}} - \nu_{\text{OCO}}^{\text{sym}}$, in the 1600–1300 cm^{-1} IR region. This is because for bidentate and bridge (monodentate) states $\Delta\nu$ is expected to be smaller (greater) than for the free formate ion, for which $\Delta\nu \approx 200\text{--}220 \text{ cm}^{-1}$.^{18,33} On the basis of this criteria, Busca and Lorenzelli's literature review suggests that bridge formates are by far the most common and stable configuration on metal oxides. The measured $\Delta\nu$ values are not always conclusive, but other vibrational frequencies of formates such as those associated with C–H bonds are less sensitive to the way species anchor to the surface particularly because neither the C atom nor the H atom is directly bound to the surface. Moreover, there is a troublesome overlap between the C–H stretching mode and the IR combination band attributed to the $\nu_{\text{OCO}}^{\text{asym}}$ and the bending of the C–H bond, all of which show up in the 2950–2800 cm^{-1} range.

Specifically, for ceria surfaces, Onishi and co-workers have identified formate species upon adsorption and decomposition of HCOOH, CH₃OH, and HCHO over dehydroxylated high-surface-area ceria powders.²⁹ For example, monodentate ($\Delta\nu \approx 351 \text{ cm}^{-1}$) and bidentate ($\Delta\nu < 250 \text{ cm}^{-1}$) species were proposed to be formed upon adsorption of HCOOH at room temperature, but the former was less stable with increasing temperature. Moreover, on the fully oxidized CeO₂(111) surface, Senanayake et al.³⁴ have argued that HCOOH dissociates to form hydroxyl groups and more likely monodentate than bidentate or bridge formates because of the crowding by surface O ions; for example, a bidentate configuration would increase the coordination of surface Ce ions from seven to nine (eightfold in bulk CeO₂). This is consistent with the rationale behind the monodentate assignment by Stubenrauch et al.³⁵ for formates on CeO₂(111) derived from HCOOH ($\Delta\nu = 220 \text{ cm}^{-1}$). However, Siokou and Nix³⁶ identified both monodentate ($\Delta\nu = 316 \text{ cm}^{-1}$) and

bidentate ($\Delta\nu = 222 \text{ cm}^{-1}$) formates upon interaction of CH₃OH with a thin CeO₂(111) film. In any case, it must be kept in mind that the vibrational modes of a chemisorbed formate species on oxide surfaces not only depend on its adsorption geometry but also on the presence of surface oxygen vacancies, nearby surface hydroxyl groups, and hydrogen bonding.^{37,38} Therefore, for the interpretation of the IR spectra in ceria-based systems, it is advantageous to analyze simultaneously the features in the spectra resulting from the formate species together with those associated with hydroxyl groups as well as the presence of reduced Ce³⁺ ions mainly attributed to oxygen vacancies. Yet, the local distribution of hydroxyl groups and oxygen vacancies can hardly be determined, if at all, experimentally on the surface of real (powder) ceria-based catalysts. Thus, creating and evaluating experimental and theoretical model catalysts that mimic the real ones in their complexity become essential for a fundamental understanding of vibrational spectra in catalysis by ceria.

Gordon et al.³⁷ investigated the structure and bonding of formic acid and formate on fully oxidized and reduced CeO₂(111) using a combined experimental (reflection absorption IR spectroscopy under ultrahigh vacuum conditions) and theoretical approach. The latter was based on density functional theory (DFT), including an effective local two-electron–one-center repulsion U_{eff} term, DFT+ U ,^{39–41} to properly describe the localization of the Ce 4f states that occurs with the reduction of Ce⁴⁺ to Ce³⁺.^{42–44} The observed O–C–O stretching modes were well-represented by a bridge configuration in which the two formate oxygen atoms are bonded to two adjacent Ce atoms on the oxidized surface ($\Delta\nu = 206/232\text{--}277 \text{ cm}^{-1}$ calc./exp. (250 K)) and by one or two vacancy-stabilized bridge states in which the formate oxygen atoms heal one or two neighboring oxygen vacancies on the reduced surface ($\Delta\nu = 315$ or $258/298\text{--}275 \text{ cm}^{-1}$ calc./exp. (250 K)), all with a coadsorbed hydrogen atom. The calculated $\Delta\nu$ values are found to be rather sensitive to the presence of hydroxyl groups and oxygen vacancies, which is particularly reflected in the multitude of $\nu_{\text{OCO}}^{\text{asym}}$ peaks spread over an observed range of up to 80 cm^{-1} . A monodentate formate state on the oxidized surface was found to be a saddle point on the local potential energy surface and higher in energy than the isolated bridge state by 0.44 eV.

Vayssilov et al.⁴⁵ studied the interaction of formate species using a Ce₂₁O₄₂ cluster and DFT+ U , with the aim of simulating CeO₂ nanostructuring in powder catalysts. They found various stable configurations that were all of the bridge type (cf. Figure 1). Most of them have the two oxygen atoms of the formate coordinated to a pair of neighboring cerium cations, and some have one or both oxygen atoms bound to two cations simultaneously. However, they pointed out that the one vacancy-stabilized bridge state reported by Gordon et al.³⁷ spontaneously transformed into other bridgelike species during geometry optimization, probably because of the higher flexibility of the Ce₂₁O₄₂ cluster compared to CeO₂(111).

More recently, Mei⁴⁶ newly investigated the bonding of formate species on fully oxidized CeO₂(111) and reported three stable configurations. The two most stable structures (within 0.05 eV) were referred to as monodentate ($\Delta\nu = 265 \text{ cm}^{-1}$) and bridge ($\Delta\nu = 247 \text{ cm}^{-1}$), the latter with the two oxygen atoms of the formate coordinated to a pair of neighboring cerium cations. Actually, their geometries are very similar, which is at variance with the expected geometrical differences between monodentate and bridge states (cf. Figure

1). The only difference lies in the O–Ce bond lengths: 2.57 and 2.75 Å (monodentate) and 2×2.61 Å (bridge). The least stable structure (by 0.45 eV) corresponds to an unusual formate triple-bonded to the surface, with two oxygen atoms of the formate coordinated to a pair of neighboring cerium cations and the carbon atom coordinated to a surface oxygen anion. Though the latter state was characterized by a $\Delta\nu$ value of 228 cm^{-1} that is within the expected range for (true) bridge states, both $\nu_{\text{OCO}}^{\text{asym}}$ and $\nu_{\text{OCO}}^{\text{sym}}$ were much smaller (by ~ 300 cm^{-1}) than the corresponding typically observed frequencies.

To summarize, on ceria surfaces the theoretically predicted most stable formate structures are generally of the bridge type, whereas monodentate species are either found to be unstable or not considered at all. Moreover, the effect of neighboring hydroxyl groups and of oxygen vacancies on the stability of formate species has only been scarcely investigated. However, in the WGS and steam-reforming of alcohols reactions over ceria, the presence of OH groups and O vacant sites are unavoidable.

The present investigation seeks to further clarify the nature of formate species on CeO_2 surfaces by using a combination of in situ transmission infrared spectroscopy during temperature-programmed surface reaction (TPSR) of methanol over a high-purity CeO_2 powder and DFT+*U* calculations of formate adsorption on oxidized and partially reduced $\text{CeO}_2(111)$ with varying concentration of coadsorbed hydroxyl groups. Statistical thermodynamics is used to determine the surface structure and composition in thermodynamic equilibrium with an environment containing methanol, water, and hydrogen at a given temperature and pressure. Further, we correlate the stability of formate species on the model $\text{CeO}_2(111)$ and their calculated vibrational properties with those observed during the methanol decomposition reaction on a CeO_2 powder. In doing this, we have been able to provide an interpretation of the nature of the observed formate species.

2. METHODS AND MODELS

2.1. Experiments. **2.1.1. Materials.** High-purity CeO_2 was prepared avoiding the use of any indecomposable salt that can leave traces of chloride, sulfate, phosphate, sodium, or potassium ions, among others. Cerium(III) nitrate hexahydrate supplied by Aldrich (99.99% Ce) was employed as ceria precursor. Solid $\text{Ce}(\text{OH})_3$ was first precipitated by the dropwise addition of the nitrate solution to an ammonia solution while controlling the pH at 8.5 with further incorporation of NH_4OH when needed. The solid was then washed for nitrate ammonium removal, dried (393 K and 12 h) and calcined in synthetic air (773 K and 4 h). The obtained pure CeO_2 powder had a specific surface area equal to 57 m^2/g (measured by the Brunauer–Emmett–Teller method) with average ~ 10 nm crystalline domains of cubic fluorite type structure (determined by X-ray diffraction and high-resolution electron microscopy). For preparation and characterization details see, for example, refs 47 and 48.

2.1.2. TPSR Experiments. In situ transmission infrared spectroscopy was used to study the temperature-programmed surface reaction (TPSR-IR) of methanol over the CeO_2 powder. A self-supported wafer of CeO_2 (~ 30 mg, diameter = 13 mm, pressed at 5 tons cm^{-2}) was located in a glass IR cell with NaCl refrigerated windows connected to a gas flow system. Before each adsorption experiment, each sample was cleaned following the reduction–oxidation procedure described in ref 47 in order to remove the surface water and carbonate species resulting from atmospheric contamination. For

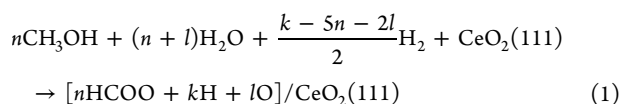
methanol adsorption, a 4% v/v CH_3OH (Merck, 99.9%)/He gas streamflow was admitted through the IR cell at 373 K during 15 min. The excess of the surface-adsorbed methanol was then removed by flowing He for 15 min at 373 K. The TPSR-IR experiment was performed by heating the IR cell up to 723 K at 5 K min^{-1} under He flow. The gas flow was 60 $\text{cm}^3 \text{min}^{-1}$ in each case. Infrared transmission spectra were recorded on a Nicolet 8700 FT-IR spectrometer with a cryogenic MCT detector, at 4 and 0.5 cm^{-1} resolution (50 scans averaged for each spectrum). Background correction of the spectra was carried out by subtracting the spectra of the pretreated cleaned wafer at each temperature. Lorentzian and/or Gaussian function sums were used to fit the overlapped bands and to measure peak areas and/or intensities.

Additionally, methanol chemisorption and TPSR using mass spectrometry to detect desorbing gaseous products (TPSR-MS) were performed in the tubular microreactor coupled online to a quadrupole mass spectrometer (Balzers QMG 112A). An amount of sample equivalent to 10 m^2 of CeO_2 was placed into the reactor and pretreated for cleaning and methanol chemisorption, following the procedure described above for the IR experiments. During the TPSR-MS experiment up to 723 at 5 K min^{-1} , the following species were scanned: CH_3OH ($m/z = 31$), CH_2O (formaldehyde, $m/z = 29$), CH_3OCH_3 (dimethyl ether, $m/z = 45$), CO ($m/z = 28$), CO_2 ($m/z = 44$), H_2O ($m/z = 18$), and H_2 ($m/z = 2$).

2.2. Theory. Spin-polarized DFT calculations were carried out using the slab–supercell approach,⁴⁹ with the Vienna Ab-initio Simulation Program (VASP, version 5.2.12).^{50–54} We treated explicitly the Ce (4f, 5s, 5p, 5d, 6s), O (2s, 2p), C (2s, 2p), and H (1s) electrons as valence states within the projector augmented wave (PAW) method⁵⁵ with a plane-wave cutoff energy of 400 eV, whereas the remaining electrons were considered as part of the atomic core. The energies and forces were calculated using the DFT+*U* approach by Dudarev et al.⁵⁶ ($U_{\text{eff}} = U - J = 4.5$ eV for the Ce 4f electrons) with the generalized gradient approximation (GGA) proposed by Perdew, Burke, and Ernzerhof (PBE).⁵⁷

The $\text{CeO}_2(111)$ surface was modeled by three O–Ce–O trilayers terminated by threefold coordinated O atoms with calculated CeO_2 bulk equilibrium lattice constant (5.485 Å) and 24 Å of vacuum between consecutive slabs. The surface unit cell and the two bottom trilayers were kept fixed during geometry optimization, whereas the rest of the atoms were allowed to fully relax. In a few test calculations, it was found that the relaxation of the middle trilayer barely affects the adsorption geometries and energies. All the calculations were performed employing a ($2\sqrt{3} \times \sqrt{3}$) surface unit cell, with a Γ -centered $2 \times 4 \times 1$ k-point mesh selected using the Monkhorst–Pack method.⁵⁸

The decomposition and reaction of CH_3OH over CeO_2 entails the release of H atoms and the formation of hydrogen, H_2 , and various dehydrogenation products such as methoxy, CH_3O , and formaldehyde, CH_2O , which either desorb together with H_2O or are further dehydrogenated to formyl, CHO, and CO. Moreover, these dehydrogenated products can be oxidized into species such as formates, HCOO, carbon dioxide, CO_2 , and carbonates, CO_3 . The nature of the formate species formed during the TPSR-IR experiment reported here will be affected by the concentration and nature of neighboring hydroxyl groups and the presence of oxygen vacancies caused by the consumption of surface oxygen. To mimic the real systems in their complexity, we have considered the reaction



and assumed thermodynamic equilibrium of chemisorbed formate species with independent reservoirs of CH_3OH , H_2O , and H_2 , i.e., gases not interacting with each other. A given (n, k, l) set defines the stoichiometry of possible local minima of the potential energy surface of the adsorbate/surface system. n ($n = 0, 1$) is the number of HCOO formate species, whereas k ($0 \leq k \leq 12$) and l ($-2 \leq l \leq 6$) are the numbers of H and O atoms, respectively, of the coadsorbed species such as water (in the dissociated or molecular form). Negative l values ($l = -1, -2$) correspond to the presence of surface oxygen vacancies and $n = k = l = 0$ to the fully oxidized $\text{CeO}_2(111)$ surface.

For each set of (n, k, l) values, we have selected various possible initial configurations and carried out full geometry optimizations until the forces acting on each atom of the adsorbed species and of the top O–Ce–O trilayer were smaller than $0.02 \text{ eV}/\text{\AA}$. For the lowest energy structure of a given (n, k, l) set, we approximate the change in the Gibbs free energy per unit area, $\Delta G_{n,k,l}$ accompanying the reaction (cf. eq 1) by

$$\Delta G_{n,k,l} \simeq \frac{1}{A} \left[\Delta E_{n,k,l} - n\Delta\mu_{\text{CH}_3\text{OH}} - (n + l)\Delta\mu_{\text{H}_2\text{O}} - \frac{k - 5n - 2l}{2}\Delta\mu_{\text{H}_2} \right] \quad (2)$$

where

$$\Delta E_{n,k,l} = E_{n,k,l} - E_{\text{CeO}_2(111)} - nE_{\text{CH}_3\text{OH}} - (n + l)E_{\text{H}_2\text{O}} - \frac{k - 5n - 2l}{2}E_{\text{H}_2} \quad (3)$$

and

$$\Delta\mu_i = \mu_i(T, p_i) - \mu_i(T, p_i^0) \quad (4)$$

In eq 3, $E_{n,k,l}$, $E_{\text{CeO}_2(111)}$, $E_{\text{CH}_3\text{OH}}$, $E_{\text{H}_2\text{O}}$, and E_{H_2} correspond to the total DFT+ U energies of the lowest energy structure of the (n, k, l) set, the clean $\text{CeO}_2(111)$ surface, and the gas-phase CH_3OH , H_2O , and H_2 species, respectively. In eq 4, $\mu_i(T, p_i)$ is the chemical potential of species i in a reservoir characterized by a temperature T and pressure p_i , and $p_i^0 = 1 \text{ atm}$. For any given value of T , smaller $\Delta\mu_i$ values correspond to smaller pressures of the reservoir of the species i .⁵⁹ In eq 2, the term $\Delta\mu_i$ accounts for the Gibbs free energy cost of removing a species i from the corresponding reservoir at (T, p_i) , and A is the area of the $(2\sqrt{3} \times \sqrt{3})$ unit cell. Equation 2 is approximate because it equates the difference of the solid Gibbs free energies by the corresponding difference of their total energies. As such, it neglects the (expected small) free energy contributions that arise predominantly from the change of adsorbate vibrational properties upon adsorption.⁵⁹ With the present definitions, for a given set of values $\Delta\mu_{\text{CH}_3\text{OH}}$, $\Delta\mu_{\text{H}_2\text{O}}$, $\Delta\mu_{\text{H}_2}$, the thermodynamically stable structure is the one with the lowest ΔG value.

We note here that there are multiple local minima with respect to the distribution of Ce^{3+} ions relative to oxygen vacancies and hydroxyl groups resulting from surface hydrogenation.^{44,60,61} The large number of defective and non-defective structures considered in this work, with or without

adsorbed formate ions and under various hydrogenation/hydroxylation levels, makes the systematic search of the global minimum energy structure with respect to the locations of the Ce^{3+} ions a very computationally demanding task. Hence, we have, in all cases, let the optimization procedure find a local minimum structures for a given starting geometry without preparing it beforehand for specific locations of the Ce^{3+} sites. However, if there is an energetically more favorable distribution of the Ce^{3+} ions with respect to the oxygen vacancies and/or hydroxyl groups than the local minimum structure found, then it is expected to affect all structures with the same composition in similar ways. Consequently, no real significant changes are expected for the presented phase diagrams below with respect to the nature of the species such as bridge**, bridge*, bridge, mono, and so on in the single-phase regions of the diagrams. Only minor changes in the positions of the lines separating the single-phase regions may occur, which are nevertheless combined with those related to accuracy in DFT as mentioned below.

Equation 2 represents a hyperplane in the 4D space spanned by $\Delta\mu_{\text{CH}_3\text{OH}}$, $\Delta\mu_{\text{H}_2\text{O}}$, $\Delta\mu_{\text{H}_2}$, and ΔG . It is important to note that for any given pair of $(\Delta\mu_{\text{H}_2\text{O}}, \Delta\mu_{\text{H}_2})$ values the resulting relative stability of two structures involving the same number of formate species per unit area does not depend on the actual $\Delta\mu_{\text{CH}_3\text{OH}}$ value. Hence, for comparing the stability of the various possible formate structure with one formate, it is possible to take a fixed value of $\Delta\mu_{\text{CH}_3\text{OH}}$, which must be large enough to allow adsorbate structures involving formates to be stable; for too low $\Delta\mu_{\text{CH}_3\text{OH}}$ values, the thermodynamically stable structures have no chemisorbed formates. After fixing a value of $\Delta\mu_{\text{CH}_3\text{OH}}$, eq 2 allows us to associate each structure to a plane in the 3D space spanned by $\Delta\mu_{\text{H}_2\text{O}}$, $\Delta\mu_{\text{H}_2}$, and ΔG . Projecting the planes characterized by the lowest value of $\Delta G(\Delta\mu_{\text{H}_2\text{O}}, \Delta\mu_{\text{H}_2})$ on the $(\Delta\mu_{\text{H}_2\text{O}}, \Delta\mu_{\text{H}_2})$ -plane results into a 2D phase diagram, which shows the thermodynamically most stable structure for each $(\Delta\mu_{\text{H}_2\text{O}}, \Delta\mu_{\text{H}_2})$ pair. Equation 4 can be used to translate $\Delta\mu_i$ into a pressure scale (p_i) at a given temperature or vice versa. Here, it is important to mention that the well-known PBE gradient approximation tendency to overestimate binding energies means that the chemical potential could be shifted within a few tenths of electronvolts. Hence, the absolute pressures might be in error by up to 2–3 orders of magnitude. Nevertheless, the general stability trend is valid. Furthermore, during a typical TPSR experiment, the surface of the CeO_2 catalyst powder is not in thermodynamic equilibrium, with independent reservoirs of CH_3OH , H_2O , and H_2 characterized by well-defined gas pressures. Nevertheless, we expect that the DFT modeling in combination with statistical thermodynamics will enable insights into the nature of formate species in the decomposition and reaction of methanol over ceria surfaces. Accordingly, in section 3, we will consider $\Delta\mu_{\text{CH}_3\text{OH}}$, $\Delta\mu_{\text{H}_2\text{O}}$, and $\Delta\mu_{\text{H}_2}$ values that are likely to represent those in the experiment and analyze the stable structures and their IR spectra in comparison with the experimental information. The computed IR vibrational frequencies have been calculated by diagonalizing the Hessian matrix. The elements of the Hessian matrix were obtained from finite differences of the DFT+ U forces with small displacements of all of the atoms allowed to relax.

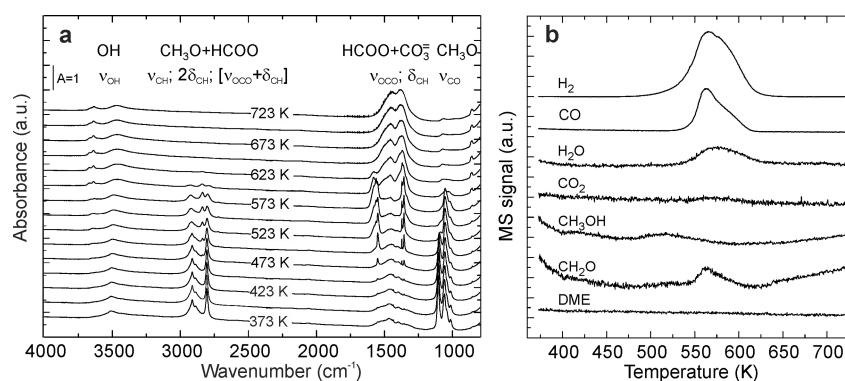


Figure 2. (a) Infrared and (b) mass spectra of surface and desorbed species, respectively, recorded during the temperature-programmed surface reaction (TPSR) of methanol on CeO_2 powder under He flow. Initial conditions: methanol adsorption at 373 K, 15 min (4% v/v $\text{CH}_3\text{OH}/\text{He}$), and heating rate = 5 K min^{-1} .

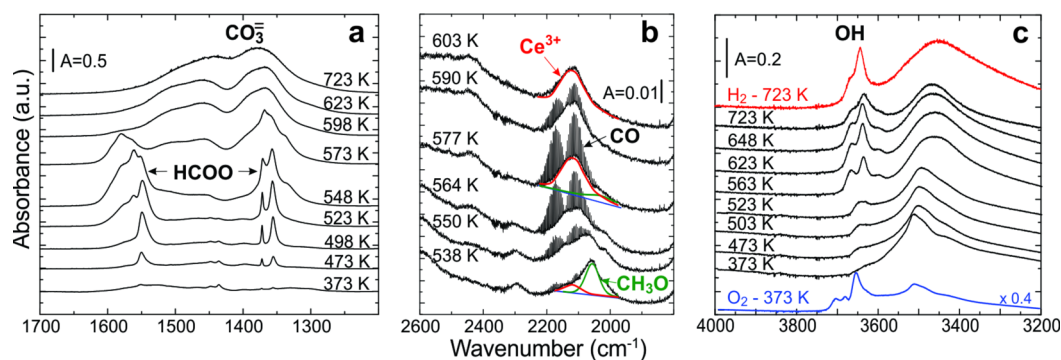


Figure 3. Details of the IR spectra evolution in the selected regions for (a) formates, (b) Ce^{3+} , and (c) hydroxyl species during the TPSR-IR experiments. The spectra of clean ceria were subtracted at each temperature in a and b. Blue and red spectra in c (without background correction) correspond to CeO_2 during the cleaning procedure (that is, before the CH_3OH adsorption) under oxidizing (O_2 at 373 K) and reducing (H_2 at 723 K) conditions.

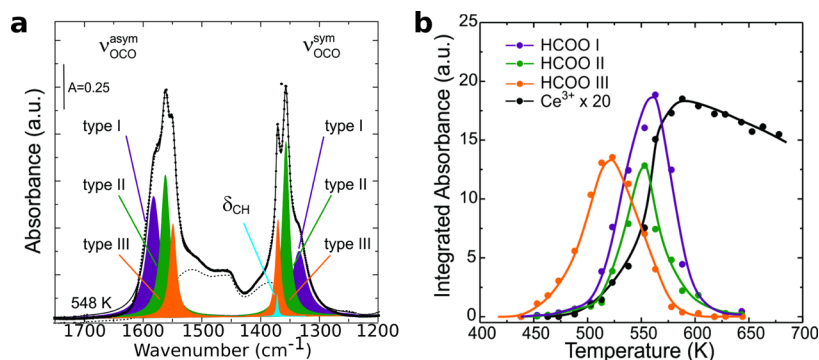


Figure 4. (a) Deconvoluted IR spectrum and band assignment for formate species types I–III on CeO_2 powder. The dots correspond to the experimental spectrum at 548 K under He flow. $\nu_{\text{OCO}}^{\text{asym}}$ and $\nu_{\text{OCO}}^{\text{sym}}$ stand for the asymmetric and symmetric O–C–O stretching mode, respectively, and δ_{CH} stands for the CH bending mode. (b) Thermal evolution of the integrated IR signals for formate and Ce^{3+} species during the TPSR-IR experiment of methanol on CeO_2 powder. Experimental conditions are the same as those described in the caption of Figure 2.

3. RESULTS AND DISCUSSIONS

3.1. Experimental Results. Upon exposure of the CeO_2 powder sample to methanol at 373 K, methoxy (CH_3O) groups form on the surface as indicated by the signal corresponding to the C–H and C–O stretching bands observed in the 2900–2700 and 1100–1010 cm^{-1} regions, respectively, of the recorded TPSR-IR spectra (Figure 2a). The intensity of the signal corresponding to the methoxy species starts decreasing around 450 K, i.e., when the typical features of formate species appear (IR signals within the 1600–1300 cm^{-1} range), and they almost disappear around 550–600 K. This observation suggests

that between 450 and 550 K methoxy groups decompose giving rise to formate species on the surface. The further release of H atoms from methoxy species reduces the catalyst surface, resulting in the formation of Ce^{3+} ions. Finally, chemisorbed carbonate groups, CO_3 , (Figure 2a) as well as CH_2O , H_2O , CO, and H_2 desorbing molecules detected through the TPSR-MS experiment (Figure 2b) are typical products of further decomposition and reaction above 550 K. This general picture is already known and has been reported in several previous works.^{37,62–64} The CH_2O and H_2O desorbing molecules clearly point to the oxidation of the dissociatively chemisorbed

CH₃OH.⁶⁵ Actually, the entire catalytic cycle for methanol oxidation reaction proceeds according to the Mars–van Krevelen mechanism, with the reactant being oxidized by lattice oxygen ions at the catalyst surface, which is in turn reduced by oxygen vacancy formation followed by a fast reoxidation step. In what follows, we will try to elucidate experimentally (and also theoretically in section 3.2) the nature of the formate species that are produced along the methanol decomposition and reaction over ceria.

Figure 3 shows in detail the three most relevant IR regions to investigate the possible formate structures and the role of neighboring hydroxyl and Ce³⁺ species: (a) 1700–1300 cm⁻¹, which contains the $\nu_{\text{OCO}}^{\text{sym}}$ and $\nu_{\text{OCO}}^{\text{asym}}$ stretches as well as the C–H bending mode of formate species, δ_{CH} ,³² (b) 2400–2000 cm⁻¹, where a small band associated with Ce³⁺ ions develops,^{66,67} and (c) 3800–3200 cm⁻¹, which displays the O–H stretching bands.⁶⁷

The deconvolution applied to solve the overlapping bands in the 1700–1300 cm⁻¹ region of the IR spectrum recorded at 548 K (Figure 3a) is shown in Figure 4a. Three ν_{OCO} IR bands were resolved and associated with formate species chemisorbed in three different ways and/or environments. In what follows, these three formate species will be referred to as formate type I, II, and III according to their decreasing $\nu_{\text{OCO}}^{\text{asym}}$ values (at 548 K): 1580, 1561, and 1550 cm⁻¹, respectively.

Because the surface Ce³⁺ IR band due to an electronic forbidden transition ${}^2F_{5/2} \rightarrow {}^2F_{7/2}$ at ~ 2120 cm⁻¹^{66,67} appears around $T \sim 500$ K (cf. Figure 3b), it is interesting to investigate a possible correlation between the thermal evolution of the three formate species mentioned above and that of the Ce³⁺ signal. Therefore, the integrated absorbance spectra assigned to formates of type I, II, and III, were plotted together with that of the Ce³⁺ band in Figure 4b as a function of temperature. The signals of the type-I, -II, and -III formates evolve differently with temperature. The type-III formate is the one that appears at the lowest temperature (slightly below ~ 450 K), i.e., before there is any significant evidence of Ce³⁺ ions. Thus, the type-III formate species is assigned to those stable on a fully oxidized ceria surface. In fact, the Ce³⁺ signal commences approximately at the temperature for which both type-II and -I formates appear, i.e., above 500 K. For that reason, in contrast to the type-III formate, type-II and -I formates are expected to be stable on partially reduced ceria by the H atoms released from the CH₃O groups that evolve into HCOO during reaction but before desorption of appreciable amounts of H₂O and H₂, starting at ~ 550 K (cf. Figure 2b).

In view of the previous discussions, it is also important to investigate any possible correlation between the thermal evolution of formates with that of hydroxyl groups. Figure 3c shows a zoom of the traditional frequency region of the IR spectra of hydroxyl bands during the TPSR experiment. After methanol exposure, at 373 K, the broad OH band around 3500 cm⁻¹ may partly correspond to hydrogen-bonded OH species⁶⁷ that result from the dissociative adsorption of methanol. After raising the temperature to approximately 600 K, this broad band shifts to lower frequencies while increasing its intensity, probably as a consequence of further dehydrogenation of CH₃O species. At the same time, three other higher-frequency bands were also detected with frequencies located at about at 3670, 3640, and 3600 cm⁻¹, respectively, similar to the ones reported by Lavalley and co-workers⁶⁸ after exposing CeO₂ to water vapor. The bands were previously assigned to isolated OH groups protruding over the surface (groups whose oxygen

atoms do not belong to the oxide lattice) bonded to a different number of cations.⁶⁸ The correlation of the observed OH vibrations with those of the three types of formate species is not straightforward because the OH bands are observed during the whole methanol decomposition and reaction, even below and above the temperature range for which formate features are unambiguously identified in the IR spectra.

Finally, Table 1 summarizes the values of $\nu_{\text{OCO}}^{\text{asym}}$, $\nu_{\text{OCO}}^{\text{sym}}$, and $\Delta\nu$ for the three formate species observed and provides

Table 1. Experimental Values of the Symmetric and Asymmetric Stretching O–C–O modes, $\nu_{\text{OCO}}^{\text{sym}}$ and $\nu_{\text{OCO}}^{\text{asym}}$, and $\Delta\nu = \nu_{\text{OCO}}^{\text{asym}} - \nu_{\text{OCO}}^{\text{sym}}$ ^a

state	frequency mode (cm ⁻¹)			Ce ³⁺
	$\nu_{\text{OCO}}^{\text{asym}}$	$\nu_{\text{OCO}}^{\text{sym}}$	$\Delta\nu$	
type I	1580	1335	245	yes
type II	1561	1356	205	yes
type III	1550	1371	179	no

^aWhether Ce³⁺ ions are present is indicated in the right column.

information on the existence (or not) of Ce³⁺ ions coexisting with each of them. According to the criterion based on the $\Delta\nu$ values for assigning a coordination to the surface to each formate species, one might infer that type III would be a bidentate or bridge formate and type I might be monodentate whereas the assignment of type II is unclear. However, as already pointed out in section 1, such assignments based on only $\Delta\nu$ values are (even when possible) not totally conclusive. Thus, in the following subsection (section 3.2) we will try to shed some light on the identification of the three formate species observed experimentally with the help of DFT+U calculations.

3.2. Theoretical Results. **3.2.1. Hydroxylation of CeO₂(111).** As mentioned above, the anchoring of formate species on oxide surfaces is influenced by the presence of surface oxygen vacancies and nearby surface hydroxyl groups. There are two possible types of hydroxyl groups on CeO₂(111): Hydroxyl groups of the first type are protruding over the surface, i.e., groups whose oxygen atoms do not belong to the oxide lattice. In what follows, a hydroxyl group of this type will be referred to as simply OH. Hydroxyl groups of the second type can be thought as the result of the chemisorption of a H atom on a threefold-coordinated surface oxygen atom and thus it will be referred to as O_sH.

We first investigated the hydroxylation of the clean and defective CeO₂(111) surfaces without formates, i.e., $n = 0$ in eq 1. About 60 different configurations with k ($0 \leq k \leq 12$) H atoms and l ($-2 \leq l \leq 6$) O atoms forming p O_sH and q OH groups ($0 \leq p = k - q \leq 6$, $0 \leq q \leq 6$) were considered as well as a few additional ones involving not only hydroxyl groups but also molecular H₂O species. The defective CeO₂(111) surface contained one or two surface oxygen vacancies, O_{vac} ($l = -1, -2$). We considered structures with $p > q$, $p = q$, and $p < q$. The full list of configurations studied can be found in the Table S1 (also Figures S1 and S2). The resulting 2D ($\Delta\mu_{\text{H}_2\text{O}}$, $\Delta\mu_{\text{H}_2}$) phase diagram is shown in Figure 5 a.

At lowest water and hydrogen chemical potentials ($\Delta\mu_{\text{H}_2\text{O}}$ and $\Delta\mu_{\text{H}_2} \lesssim -2$ eV), i.e., for low water and hydrogen pressures at 400–600 K, the oxygen-defective CeO₂(111) surface with one and two vacancies, which produce two and four Ce³⁺ ions per unit cell, respectively (Figure 5b), is stable. When the water

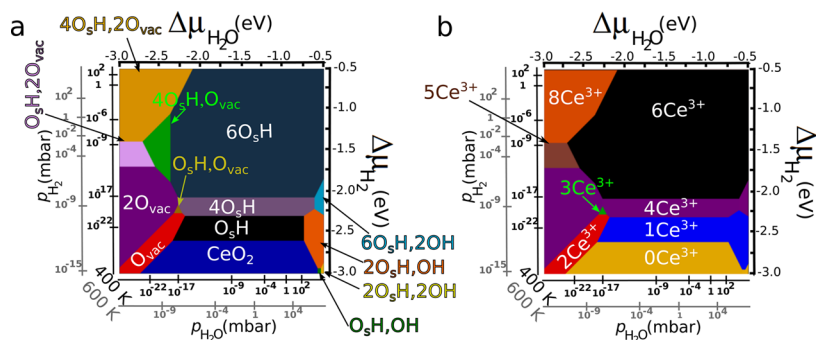


Figure 5. (a) Surface phase diagram of the hydroxylated $\text{CeO}_2(111)$ surface. (b) Phase diagram according to the number of Ce^{3+} ions per unit cell of the thermodynamically stable structures in panel a.

pressure remains low but that of hydrogen increases, defective structures with O_sH groups are stable, such as $(\text{O}_s\text{H},\text{O}_{\text{vac}})$, $(\text{O}_s\text{H},2\text{O}_{\text{vac}})$, $(4\text{O}_s\text{H},\text{O}_{\text{vac}})$, and $(4\text{O}_s\text{H},2\text{O}_{\text{vac}})$, with three, five, six, and eight Ce^{3+} ions per unit cell (Figure 5b), respectively; an isolated chemisorbed H atom and those resulting from the dissociation of H_2 produce one Ce^{3+} ion per chemisorbed H atom.⁶⁰

As the water pressure increases ($-2 \lesssim \Delta\mu_{\text{H}_2\text{O}} \lesssim -0.8$ eV), for low hydrogen pressures ($\Delta\mu_{\text{H}_2} \lesssim -2.6$ eV), the fully oxidized surface is stable, whereas upon increasing the hydrogen pressure, nondefective structures with one, four, or six O_sH groups are stable. It is only for higher water pressures ($\Delta\mu_{\text{H}_2\text{O}} \gtrsim -0.8$ eV) that various structures involving both O_sH and OH hydroxyl groups would become stable, though temperature determines the actual stability of such structures. In particular, for high water and low hydrogen pressures, the number of both types of hydroxyls are equal to each other ($p = q = 1, \dots, 5$). The stable structures with $p = q$ are in fact sets of p hydroxyl pairs ($\text{O}_s\text{H},\text{OH}$) where the O_s atom is nearest neighbor of the surface Ce atom on top of which the OH adsorbs (Figures 6 a, c–f). Such a hydroxyl pair results from the partial dissociation of a H_2O molecule and does not produce Ce^{3+} ions (Figure 5b).⁶⁹ In fact, the molecular and hydroxyl pair states are very close in energy and thus expected to coexist but not with the fully dissociated molecule, i.e., largely

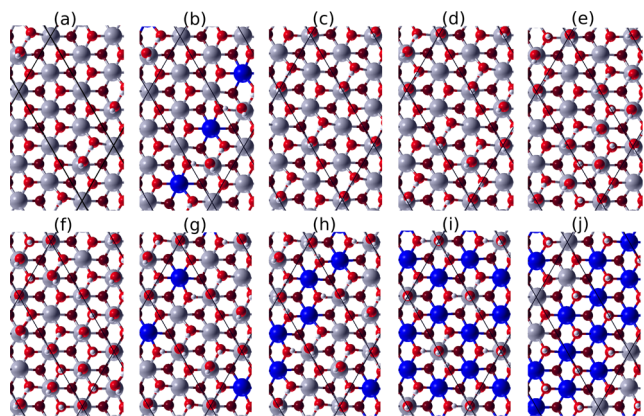


Figure 6. Thermodynamically stable structures of hydroxylated ceria without oxygen vacancies: (a) $\text{O}_s\text{H},\text{OH}$, (b) $2\text{O}_s\text{H},\text{OH}$, (c) $2\text{O}_s\text{H},2\text{OH}$, (d) $3\text{O}_s\text{H},3\text{OH}$, (e) $4\text{O}_s\text{H},4\text{OH}$, (f) $5\text{O}_s\text{H},5\text{OH}$, (g) $4\text{O}_s\text{H},3\text{OH}$, (h) $5\text{O}_s\text{H},3\text{OH}$, (i) $6\text{O}_s\text{H},2\text{OH}$, and (j) $4\text{O}_s\text{H}$. Red, dark red, and white balls stand for surface O, subsurface O, and H atoms, respectively. Ce^{4+} and Ce^{3+} ions are gray and blue, respectively.

separated O_sH and OH groups. The latter state is significantly less stable (by ~ 0.3 – 0.4 eV).⁶⁹ The geometry of $(\text{O}_s\text{H},\text{OH})$ pair (cf. Figure 6a) indicates that the H atom of the O_sH group forms a H bond with the O atom of the OH with ~ 1.67 Å distance, providing stability to the structure. This H bond entails an increase of the O_s –H equilibrium distance with respect to an isolated O_sH group: 0.97 vs 1.00 Å. In contrast, the O–H equilibrium distance for the OH group barely changes with $(\text{O}_s\text{H},\text{OH})$ pair formation. We will show below (section 3.2.3) that variations in the hydrogen bond strength are reflected in the calculated O_s –H vibrational stretching frequency.

Thermodynamically stable structures with $p > q$ (more abundant O_sH groups) consist of $q(\text{O}_s\text{H},\text{OH})$ pairs plus $(p - q)$ additional O_sH groups (cf. Figures 6b,g–i). Accordingly, the number of Ce^{3+} ions per unit cell in these structures is equal to $p - q$ (Figure 5b). In these cases, various O_sH groups tend to interact through H bonds with a single OH group, and their O_s –H equilibrium distances are increased with respect to the value for isolated hydroxyl groups, as already discussed for the case of $p = q$.

In summary, thermodynamically stable structures have either O_sH groups only ($p \neq 0$ and $q = 0$), $(\text{O}_s\text{H},\text{OH})$ pairs, i.e., structures with $p = q$, or a combination of O_sH groups with $(\text{O}_s\text{H},\text{OH})$ pairs ($p > q > 0$); there are no structures with OH groups only.

3.2.2. Formate Species on $\text{CeO}_2(111)$. We turn now our attention to the coexistence of formate (HCOO) species with hydroxyl groups and surface oxygen vacancies on $\text{CeO}_2(111)$. As mentioned in section 1, bridge formates are bound to the surface by two O atoms, which in turn are bound to one or two Ce atoms. Here, the label “bridge” is reserved for the case in which both O atoms are bound to one Ce atom, whereas bridge* and bridge** denote configurations in which one or both O atoms are bound to two Ce atom, respectively (cf. Figure 1). Because bridge* and bridge** configurations are likely to be unstable on the (oxygen-terminated) fully oxidized $\text{CeO}_2(111)$ surface, such structures have been created on the defective surface with one and two surface oxygen vacancies, respectively. Furthermore, we have also considered formate species coadsorbed with O_sH and OH hydroxyl groups (forming $(\text{O}_s\text{H},\text{OH})$ pairs or not) as well as with H_2O molecules. Hence, the labeling of the formate structures is augmented by three integer numbers p,q,r as subindexes to indicate the number of O_sH , OH, and H_2O species coadsorbed with the formate, respectively. For instance, mono_{pqr} (brg_{pqr}^{**}) will denote a structure involving a monodentate (bridge**) formate coadsorbed with p O_sH , q OH, and r H_2O species. In

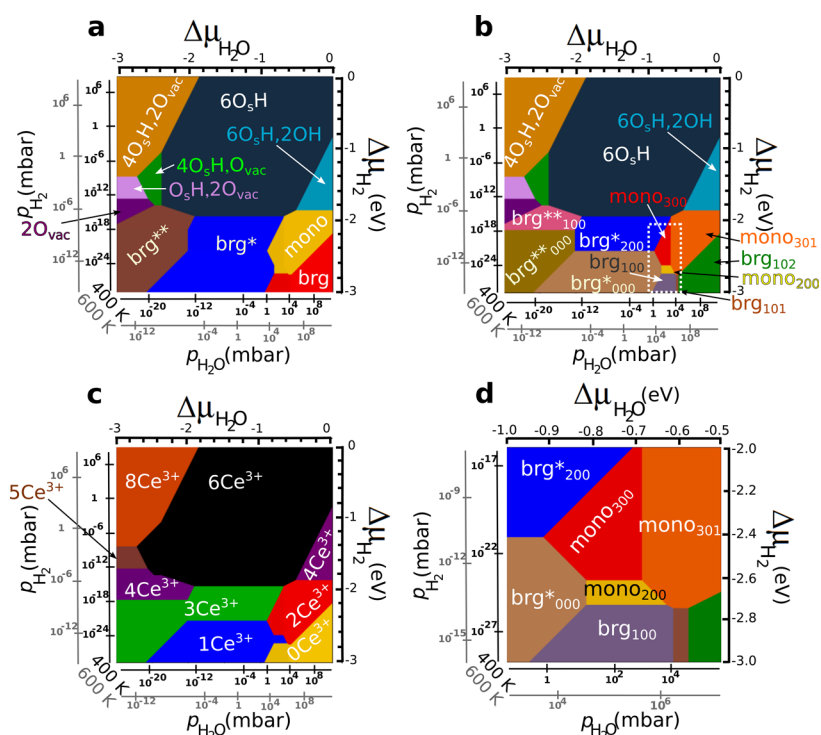


Figure 7. (a) Phase diagram according to the anchoring of the formate species in the thermodynamically stable structures in panel b. (b) Surface phase diagram of the $\text{CeO}_2(111)$ surface for $\Delta\mu_{\text{CH}_3\text{OH}} = -3$ eV. (c) Phase diagram according to the number of Ce^{3+} ions per unit cell of the thermodynamically stable structures in panel a. (d) Zoom of the rectangular region outlined in dashed white line in b.

total, we have considered about 100 different configurations. The full list of configurations studied can be found in Table S2 (also Figures S3–S7).

As explained above (section 2), the relative stability of formate structures involving the same number of formate species, does not depend on the actual $\Delta\mu_{\text{CH}_3\text{OH}}$ value (eq 2). The 2D ($\Delta\mu_{\text{H}_2\text{O}}$, $\Delta\mu_{\text{H}_2}$) phase diagram with no adsorbed formate species (cf. Figure 5a) is equivalent to that obtained for one formate ($n = 1$) and $\Delta\mu_{\text{CH}_3\text{OH}} = -10$ eV. Figure 7 shows the phase diagram for the example of $\Delta\mu_{\text{CH}_3\text{OH}} = -3$ eV, and Figure 8 displays the geometry of the thermodynamically stable formate structures. Inspection of Figure 7a,b reveals that formate species are stable for low $\Delta\mu_{\text{H}_2}$ values ($\Delta\mu_{\text{H}_2} \lesssim -2$ eV), which correspond to relatively low hydrogen pressures, i.e., $< 10^{-11}/10^{-8}$ mbar at $\sim 500/600$ K. The nature of the stable formate species varies from bridge**, bridge*, bridge, and monodentate as the water pressure changes from low to high values. As expected, the bridge** and bridge* species are not stable at high water chemical potentials for which the $\text{CeO}_2(111)$ surface is fully oxidized. Furthermore, Figure 7b shows whether the respective stable formates, “name”_{pqr} are coadsorbed with p O_5H , q OH hydroxyl groups, and/or r H_2O molecules. We find that the thermodynamically stable structures do not have OH hydroxyl groups ($q = 0$). Moreover, at a given water pressure, the number of O_5H hydroxyl groups stabilizing bridge** and bridge*-type formates increases with increasing hydrogen pressure (cf. brg^{**}_{000} and brg^{**}_{100} as well as brg^{*}_{000} and brg^{*}_{200}). An important observation extracted from Figure 7b is that on the oxidized surface the lone bridge brg_{000} formate is not thermodynamically stable; however, the bridge one coadsorbed with a neighboring O_5H hydroxyl group, brg_{100} , is, in line with the results by Overbury and co-workers.³⁷

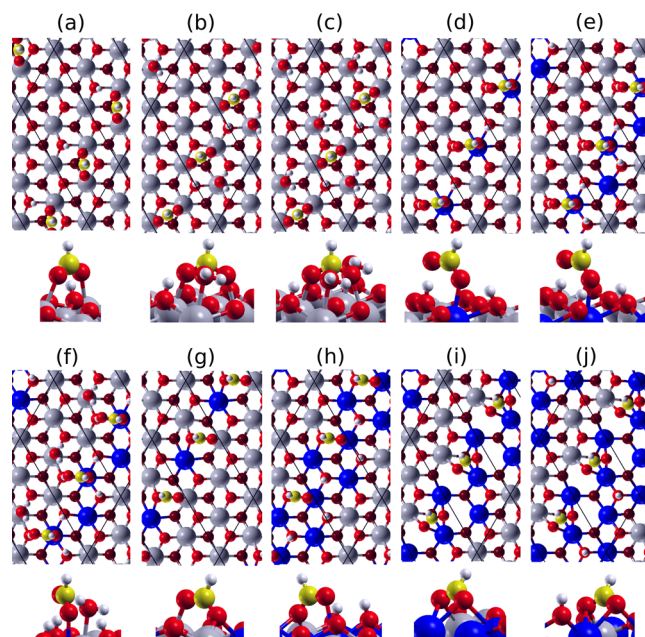


Figure 8. Thermodynamically stable formate structures as in Figure 7b: (a) brg_{100} , (b) brg_{101} , (c) brg_{102} , (d) mono_{200} , (e) mono_{300} , (f) mono_{301} , (g) brg^{*}_{500} , (h) brg^{*}_{200} , (i) brg^{**}_{500} , and (j) brg^{**}_{100} . Red, dark red, and white balls stand for surface O, subsurface O, and H atoms, respectively. Ce^{4+} and Ce^{3+} ions are gray and blue, respectively. C atoms are yellow.

Moreover, we observe that starting from the brg_{100} formate as the number of neighboring O_5H hydroxyl groups increases the number of coadsorbate brg_{p00} structures with $p > 1$ are not stable whereas monodentate structures, such as mono_{200} and mono_{300} , are. Such monodentate species are stabilized by H bonds between

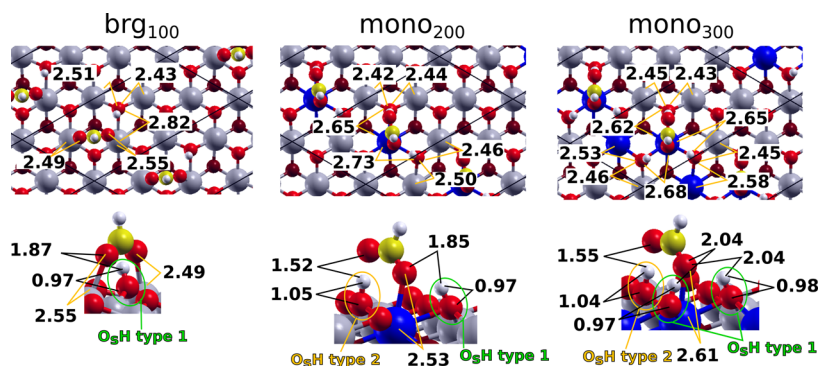


Figure 9. Geometry of the brg_{100} , mono_{200} , and mono_{300} formate structures. Selected bond lengths (in Å) are indicated.

the O atom of the formate not bound to a Ce ion and the H atoms of the surrounding O_sH groups. The fact that in previous theoretical works^{37,46} monodentate states were not reported to be stable is a simply consequence of not having considered a high enough concentration of hydroxyl groups near the formate species which is necessary if one aims to describe the stability of formates under real catalytic conditions. Finally, we note that the coadsorption of formates with one or two water molecules (cf. brg_{101} , brg_{102} and mono_{301}) or corresponding hydroxyl ($\text{O}_s\text{H}, \text{OH}$) pairs (only ~ 0.05 eV less stable) would be stable at relatively high water pressures, yet temperature determines the existence or nonexistence of such structures.

Figure 7c shows a 2D ($\Delta\mu_{\text{H}_2\text{O}}, \Delta\mu_{\text{H}_2}$) phase diagram, indicating the number of Ce^{3+} ions per unit cell for each thermodynamically stable structure. We recall that an oxygen vacancy leaves behind two Ce^{3+} ions. Moreover, the adsorption of hydrogen atoms, forming O_sH groups, is associated with one Ce^{3+} ion per hydrogen atom, and formate species carry formally one negative charge (HCOO^-), whereas molecular or hydroxyl pair adsorption of water does not produce Ce^{3+} ions. Hence, upon coadsorption of a negatively charged formate species and one O_sH hydroxyl group on the fully oxidized surface, no Ce^{4+} ions are reduced to Ce^{3+} . This is the case of bridge-type structures on the fully oxidized surface (cf. red/yellow region Figure 7a,c), namely, brg_{100} , brg_{101} , and brg_{102} (cf. Figure 7b). Moreover, for monodentate formates on the nondefective surface (cf. yellow region Figure 7a), the number of Ce^{3+} ions in the mono_{p0} structures is equal to $p - 1$, i.e., one for mono_{200} and two for mono_{300} and mono_{301} (cf. Figure 7b,c). Furthermore, the bridge* and bridge** structures on the defective surface with one and two surface oxygen vacancies, respectively (cf. Figure 7a), involve one, three, or four Ce^{3+} ions (cf. Figure 7c). For instance, in the brg_{000}^* structure, the HCOO^- formate is adsorbed on a surface with one vacancy, i.e., with two excess electrons; thus, there is one Ce^{3+} ion. Therefore, in the brg_{200}^* structure with two coadsorbed O_sH hydroxyl groups in addition there are three Ce^{3+} ions. A similar electron counting can be done for the brg_{000}^* and brg_{200}^* structures.

In the following, we will attempt to correlate the theoretical results with those of the TPRS-IR experiments (section 3.1). The important question is what is the nature of the observed type-III, -II, and -I formates that consecutively are formed upon decomposition of the methoxy groups between 450 and 550 K? To identify the region in the phase diagram of high relevance to the experiments (cf. Figure 7), we recall that when the first formate features are observed in the IR spectra the signal corresponding to Ce^{3+} ions is negligible (Figure 4); thus, type-

III formates should correspond to those stable on a fully oxidized ceria surface. Starting from type-III formates, as the temperature increases, types II and I are expected to form on a partially reduced ceria by the H atoms released from the methoxy groups. Accordingly, the lack of Ce^{3+} ions when the reaction starts prevents any of the species that are stable on a defective ceria surface, i.e., bridge* and bridge**, from being the type-III formate. Moreover, water molecules are not expected to be coadsorbed on the catalyst surface under reaction conditions, which excludes the brg_{101} , brg_{102} , and mono_{301} structures from relating to any of the observed formates. Hence, we are left with three formate structures, namely, brg_{100} , mono_{200} , and mono_{300} with one, two, and three coadsorbed O_sH hydroxyl groups, respectively. The brg_{100} structure has no Ce^{3+} ion. The stability analysis indicates that starting from the brg_{100} formate the mono_{200} and mono_{300} structures with one and three Ce^{3+} ions, respectively, would successively appear on the catalyst surface with increasing surface hydroxylation. Accordingly, we relate the observed type-III formate with the brg_{100} structure and types II and I with the mono_{200} and mono_{300} structures, respectively.

Figure 9 provides detailed information on the brg_{100} , mono_{200} , and mono_{300} formate structures. There are two types of O_sH hydroxyl groups, namely, type 1 and 2. In type 1 (2), the H atom of the O_sH group interacts with a formate O atom that is (not) bound to a surface Ce ion. The H-bond equilibrium distance, i.e., between the H atom of the O_sH group and the O atom of the formate, for type-1 groups is larger than that for type 2 (1.85–2.04 Å vs 1.52–1.55 Å), whereas the O_sH bond distance in type-1 hydroxyl groups is shorter than that in type 2 (0.97–0.98 Å vs 1.04–1.05 Å). Both results indicate that the H bonds formed between formates and type-2 O_sH groups are stronger than those involving type-1 O_sH groups. Note that the type-2 O_sH groups are also stronger than those in ($\text{O}_s\text{H}, \text{OH}$) pairs discussed above (section 3.2.1). The comparison of the mono_{200} and mono_{300} structures reveals that upon increasing the number of neighboring O_sH groups the strength of both types of H bonds tends to decrease as a consequence of the sharing of the hydroxyl–formate interaction by an increased number of hydroxyl groups. In the next subsection, we will address how hydrogen bonding of different strengths affects the stretching frequency of O_sH bonds.

3.2.3. Vibrational Frequency Analysis. To further check the plausibility of the proposed assignment of the brg_{100} , mono_{200} , and mono_{300} structures (Figure 9) to the experimentally observed type-III, -II, and -I formates, respectively, we have carried out vibrational frequency calculations (cf. Tables S3–

Table 2. Calculated and Measured Symmetric and Asymmetric O–C–O Stretching Frequencies, $\nu_{\text{OCO}}^{\text{sym}}$ and $\nu_{\text{OCO}}^{\text{asym}}$, Respectively, as Well as the Difference between Them, $\Delta\nu^a$

name	exp. type I	theo. mono ₃₀₀	diff.	exp. type II	theo. mono ₂₀₀	diff.	exp. type III	theo. brg ₁₀₀	diff.
Ce ³⁺	yes	yes		yes	yes		no	no	
$\nu_{\text{OCO}}^{\text{asym}}$ (cm ⁻¹)	1580	1568	+12	1561	1548	+13	1550	1542	+8
$\nu_{\text{OCO}}^{\text{sym}}$ (cm ⁻¹)	1335	1325	+10	1356	1336	+20	1371	1355	+16
$\Delta\nu$ (cm ⁻¹)	245	243	+2	205	212	-7	179	187	-8

^aDifferences between the experimental and theoretical results are also listed.

S5). In Table 2, we only compare the theoretical frequencies of the O–C–O symmetric and asymmetric stretching modes of the brg₁₀₀, mono₂₀₀, and mono₃₀₀ structures with the experimental values corresponding to type-III, -II, and -I formates, respectively. Interestingly enough, the calculated $\nu_{\text{OCO}}^{\text{asym}}$ and $\nu_{\text{OCO}}^{\text{sym}}$ values for the brg₁₀₀, mono₂₀₀, and mono₃₀₀ structures are in good agreement with those experimentally observed for the type-III, -II, and -I formates, respectively, with deviations not larger than 20 cm⁻¹. Discrepancies are even smaller between the corresponding $\Delta\nu$ values, presumably because of a partial cancellation of errors. Thus, the vibrational frequency analysis further supports the proposed association between the experimental type-III, -II, and -I formates with the brg₁₀₀, mono₂₀₀, and mono₃₀₀, respectively. Moreover, we note that the bridge ($\Delta\nu < 190$ cm⁻¹) and monodentate bonding ($\Delta\nu > 190$ cm⁻¹) are distinguishable by the measured splitting. Furthermore, we observe a change of about 40 cm⁻¹ between the mono₂₀₀ and mono₃₀₀ structures and conclude that the value of $\Delta\nu$ can be influenced by the environment of the formate as well as by hydrogen bonding.

In contrast to the generally accepted view that bridge formates are the most common and stable configuration on metal oxides (cf. section 1), we here report the stability of monodentate formates species for a relatively high concentration of hydroxyl species compatible with usual experimental conditions. The stability of such species is due, to a great extent, to the (strong) H bonds formed between the formates and the type-2 O_sH groups, as discussed above. Then, it is worth elucidating whether the corresponding softened O_s–H stretching gives rise to a distinct IR signal not overlapping with the many (often broad) bands associated with hydroxyl groups (cf. Figure 3c), favoring its experimental detection. Accordingly, we have computed the O–H stretching frequencies for the brg₁₀₀, mono₂₀₀, and mono₃₀₀ formate structures (cf. Figure 9) as well as for the thermodynamically stable structures for the hydroxylated nondefective ceria surface without coadsorbed formates (cf. Figure 6). Figure 10 summarizes those results. On the hydroxylated surface (no formates), two groups of high-frequency stretching modes between 3800 and 3700 cm⁻¹ are obtained. They correspond to OH groups within (O_sH,OH) pairs and isolated O_sH hydroxyl groups, i.e., those not forming hydroxyl pairs (black bars). They are slightly higher than (but still consistent with) the IR peaks in the 3730–3650 cm⁻¹ region (cf. blue spectrum in Figure 3c) recorded before exposing the surface to methanol but having the unavoidable presence of water dissociation products, i.e., OH and O_sH. The lower lying O–H stretch frequency modes between 3600 and 2750 cm⁻¹ (Figure 10, black bars) correspond to O_sH groups forming H bonds that are differently arranged depending on the surface concentration of hydroxyl groups. They can be associated with the IR band roughly centered at ~3500 cm⁻¹ observed experimentally for

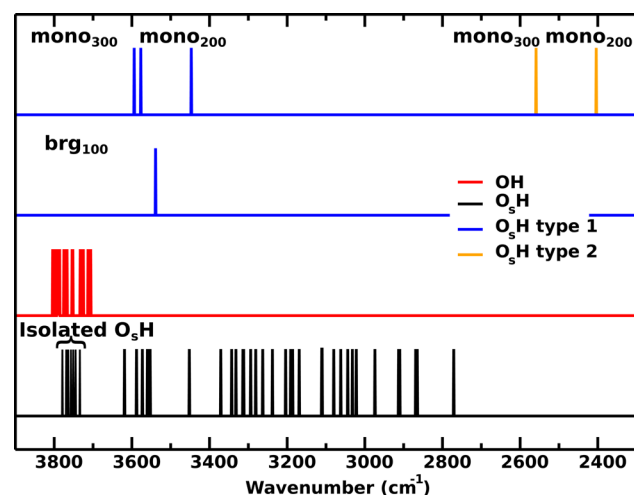


Figure 10. O–H stretching frequencies for hydroxylated surface structures without coadsorbed formates (bottom panel) and for the brg₁₀₀, mono₂₀₀, and mono₃₀₀ formate structures (middle and top panels). Black bars correspond to O_sH groups, which could form H bonds with other hydroxyl groups. Red bars correspond to OH groups forming (O_sH,OH) pairs; blue and yellow bars correspond to type-1 and type-2 O_sH groups, respectively.

hydroxylated ceria surfaces (cf. Figure 3c, blue spectrum) and attributed to hydroxyl groups forming H bonds by Lavalley and co-workers,⁶⁷ in line with the present and previous theoretical results.⁶⁹

After identifying the frequency regions within which O–H stretching modes of hydroxyl groups without (or far from) coadsorbed formates lie, we turn to the O–H stretching of type-1 and -2 O_sH groups that stabilize the monodentate formate structures mono₂₀₀ and mono₃₀₀ (cf. upper panel of Figure 10). It is observed that stretching frequencies of type-1 O_sH groups lie between 3600 and 3440 cm⁻¹ (blue bars), so they overlap with the broad band of O_sH groups forming H bonds with other hydroxyl groups (black bars in the bottom panel). In contrast, the frequencies of type-2 O_sH groups lie between 2550 and 2400 cm⁻¹ (yellow bars), i.e., much below the frequency range of the broad band. This is related to the particularly strong H bonds formed by type-2 O_sH group with monodentate formates discussed above. Hence, our results show not only that type-2 O_sH groups are crucial for the stabilization of monodentate formates but also that they should give rise to a low-lying IR band. Interestingly, in Figure 3b, around $T = 550$ K, the appearance of a small but clearly noticeable IR broad peak at 2430 cm⁻¹ is observed. In light of our theoretical results, we suggest that this feature may be associated with the type-2 O_sH groups responsible for the stabilization of monodentate formates. The integrated absorbance of the 2430 cm⁻¹ peak as a function of temperature

(cf. Figure 11) reveals that its (low) intensity increases when the signal corresponding to type-III formates starts to decrease;

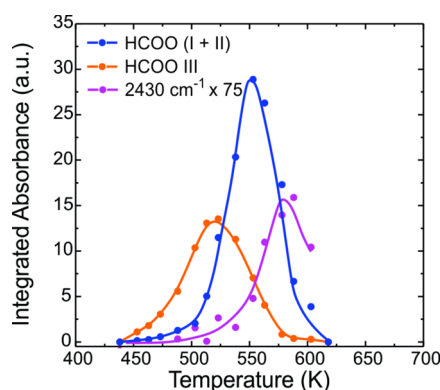


Figure 11. Thermal evolution of the integrated IR signals for formate (I+II) and III species and for the band at 2430 cm^{-1} during the TPSR-IR experiment of methanol on CeO_2 powder, recorded under He flow. Initial conditions: methanol adsorption at 373 K, 15 min (4% v/v $\text{CH}_3\text{OH}/\text{He}$), and heating rate = 5 K min^{-1} .

however, it is shifted somewhat up in temperature with respect to the signal obtained for formate types II and I. Considering that a nonvanishing intensity of the 2430 cm^{-1} peak at and above $T \sim 600\text{ K}$ could partially be due to strong H bonds between the O_sH groups and carbonates species, we take the 2430 cm^{-1} band as an additional evidence for the stabilization mechanism of monodentate species by H bonds.

We finally note that the above-discussed weakening of each individual H bond upon increasing the concentration of hydroxyl groups interacting with a single monodentate formate (section 3.2.2) is reflected in the higher stretching frequencies of both type-1 and -2 O_sH groups for the mono_{300} structure as compared to those for the somewhat less hydroxylated mono_{200} structure.

4. CONCLUSIONS

TPSR-IR experiments of methanol adsorbed on the surface of a pure ceria powder have been combined with DFT calculations for a model $\text{CeO}_2(111)$ surface to investigate the nature of the formate species that are formed during methanol decomposition and reactions affected by the presence of neighboring hydroxyl groups and oxygen vacancies resulting from the consumption of surface oxygen atoms upon reaction. At temperatures within the 450–500 K range, formates, namely type III, are adsorbed on the oxidized surface with a measured O–C–O asymmetric/symmetric ($\nu_{\text{OCO}}^{\text{asym}}/\nu_{\text{OCO}}^{\text{sym}}$) stretching frequency of $1550/1371\text{ cm}^{-1}$. As the temperature increases from 500 to 550 K, the CeO_2 surface becomes more and more hydroxylated and therefore reduced because of the decomposition of methoxy species. Type-III formates are then no longer present on these surfaces, but different formate types emerge with $\nu_{\text{OCO}}^{\text{asym}}/\nu_{\text{OCO}}^{\text{sym}}$ equal to $1561/1356$ and $1580/1335\text{ cm}^{-1}$, coded type II and I, respectively. Accordingly, theoretical models of formate species in bridge and monodentate configurations on the $\text{CeO}_2(111)$ surface were created, considering the presence of surface oxygen vacancies, hydroxyl groups, and water. The thermodynamic stability of the adsorbate structures, assuming equilibrium with independent reservoirs of CH_3OH , H_2O and H_2 , was determined.

Experimentally, formate species were initially observed in the absence of or with small amounts of Ce^{3+} ions and without molecularly coadsorbed water. These experimental conditions can be associated (within our theoretical modeling) to a H_2O chemical potential within the -0.6 to -1 eV range and to a H_2 chemical potential lower than -2 eV . Within this window of chemical potentials, for a relatively small degree of surface hydroxylation (corresponding to low pressures of the hydrogen reservoir and to 450–500 K in experiments), the stable formate species adsorbs in a bridge configuration (brg_{100}) with a neighboring surface hydroxyl group on a fully oxidized surface (no Ce^{3+}). For a higher degree of surface hydroxylation (corresponding to higher pressures of the hydrogen reservoir and to 500–550 K in experiments), monodentate formate structures coadsorbed with two (mono_{200}) and three (mono_{300}) hydroxyl groups and one and two Ce^{3+} ions, respectively, become stable. The calculated $\nu_{\text{OCO}}^{\text{asym}}/\nu_{\text{OCO}}^{\text{sym}}$ frequencies were $1542/1355$, $1548/1336$, and $1568/1325\text{ cm}^{-1}$ for the brg_{100} , mono_{200} , and mono_{300} structures in good agreement with the experimentally observed type-III, -II, and -I formate species, respectively. Clearly, the influence of the presence of oxygen vacancies and hydroxyl groups cannot be ignored when considering the stability of formate species on ceria surfaces. In particular, we find that hydroxyl groups play a crucial role in the stabilization of monodentate formate species by hydrogen bonding; thus, bridge-type bonding is not necessarily the most common formate species on ceria surfaces as previously suggested. The existence of a low-lying IR band related to the stretching of the weakened O_sH bonds of surface hydroxyl groups involved in hydrogen bonding with formates provides further support for our conclusion.

We have also demonstrated that though in situ vibrational spectroscopy offers a very powerful experimental tool box for allowing investigation of reaction intermediates on real powder catalyst surfaces the interpretation of vibrational spectra is far from trivial and the synergy between theory and experiment is essential to that end. Theoretical model studies using well-defined systems allow us to disentangle the complex vibrational spectra, and in doing this, we have been able to explain the nature of the observed formate species while bridging the gap between real and model systems.

■ ASSOCIATED CONTENT

Supporting Information

The Supporting Information is available free of charge on the ACS Publications website at DOI: [10.1021/acs.jpcc.5b05070](https://doi.org/10.1021/acs.jpcc.5b05070).

Tables of total energies, number of Ce^{3+} ions, and (n,l,k) sets eq 2, as well as top views for all structures studied. Tables of vibrational frequencies for all stable structures in the phase diagrams of Figures 5b and 7b. Table of selected bond lengths for the stable formate structures. (PDF)

■ AUTHOR INFORMATION

Corresponding Authors

*E-mail: abonivar@santafe-conicet.gov.ar.

*E-mail: busnengo@ifir-conicet.gov.ar.

Notes

The authors declare no competing financial interest.

ACKNOWLEDGMENTS

M.V.B. and A.L.B. are grateful for the financial support of the National Agency for the Promotion of Science and Technology (ANPCyT, grant PICT 2012-1280) and the Universidad Nacional del Litoral (grant CAI+D 2011 UNL, PI 501 201101 00311). M.V.G.-P. thanks MINECO (CTQ2012-32928) for financial support and BIFI-ZCAM (Universidad de Zaragoza) for computer resources, technical expertise, and assistance. P.G.L. and H.F.B. acknowledge CONICET, (Project PIP 0667) and UNR (Project PID ING235) for financial support and the CCT-Rosario Computational Center, member of the High Performance Computing National System (SNCAD, MincyT-Argentina) for allocation of computer time. The COST action CM1104 is gratefully acknowledged. We thank Damián A. Scherlis for helpful discussions.

REFERENCES

- (1) Inaba, H.; Tagawa, H. Ceria-Based Solid Electrolytes. *Solid State Ionics* **1996**, *83*, 1–16.
- (2) Trovarelli, A.; de Leitenburg, C.; Boaro, M.; Dolcetti, G. The Utilization of Ceria in Industrial Catalysis. *Catal. Today* **1999**, *50*, 353–367.
- (3) Swartz, S. L.; Seabaugh, M. M.; Holt, C. T.; Dawson, W. J. Fuel Processing Catalysts Based on Nanoscale Ceria. *Fuel Cells Bull.* **2001**, *4*, 7–10.
- (4) O'Connell, M.; Morris, M. New Ceria-Based Catalysts for Pollution Abatement. *Catal. Today* **2000**, *59*, 387–393.
- (5) Aneggi, E.; Boaro, M.; de Leitenburg, C.; Dolcetti, G.; Trovarelli, A. Insights into the Redox Properties of Ceria-Based Oxides and Their Implications in Catalysis. *J. Alloys Compd.* **2006**, *408–412*, 1096–1102.
- (6) Zhang, Q.; Wen, J.; Shen, M.; Wang, J. Effect of Different Mixing Ways in Palladium/Ceria-Zirconia/Alumina Preparation on Partial Oxidation of Methane. *J. Rare Earths* **2008**, *26*, 700–704.
- (7) Ayastuy, J.; Gurbani, A.; González-Marcos, M.; Gutiérrez-Ortiz, M. Effect of Copper Loading on Copper-Ceria Catalysts Performance in CO Selective Oxidation for Fuel Cell Applications. *Int. J. Hydrogen Energy* **2010**, *35*, 1232–1244.
- (8) Nahar, G.; Dupont, V. Hydrogen Production from Simple Alkanes and Oxygenated Hydrocarbons over Ceria-Zirconia Supported Catalysts: Review. *Renewable Sustainable Energy Rev.* **2014**, *32*, 777–796.
- (9) Song, C. Fuel Processing for Low-Temperature and High-Temperature Fuel Cells: Challenges, and Opportunities for Sustainable Development in the 21st Century. *Catal. Today* **2002**, *77*, 17–49.
- (10) Jacobs, G.; Patterson, P. M.; Graham, U. M.; Crawford, A. C.; Davis, B. H. Low Temperature Water Gas Shift: the Link Between the Catalysis of WGS and Formic Acid Decomposition over Pt/Ceria. *Int. J. Hydrogen Energy* **2005**, *30*, 1265–1276.
- (11) Trovarelli, A.; Fornasiero, P., Eds. *Catalysis by Ceria and Related Materials*, 2nd ed.; Catalytic Science Series, Vol. 12; Imperial College Press: London, 2013.
- (12) Rodríguez, J.; Liu, P.; Hrbek, J.; Evans, J.; Pérez, M. Water Gas Shift Reaction on Cu and Au Nanoparticles Supported on CeO₂(111) and ZnO(0001⁻): Intrinsic Activity and Importance of Support Interactions. *Angew. Chem., Int. Ed.* **2007**, *46*, 1329–1332.
- (13) Ilinich, O. M.; Liu, Y.; Castellano, C.; Koermer, G.; Moini, A.; Farrauto, R. A New Palladium-Based Catalyst for Methanol Steam Reforming in a Miniature Fuel Cell Power Source. *Platinum Met. Rev.* **2008**, *52*, 134–143.
- (14) Castellano, C. R.; Liu, Y.; Moini, A.; Koermer, G. S.; Farrauto, R. J. *CATALYST Composition for Alcohol Steam Reforming*. U.S. Patent: 7569511, August 4, 2009.
- (15) Yi, N.; Si, R.; Saltsburg, H.; Flytzani-Stephanopoulos, M. Active Gold Species on Cerium Oxide Nanoshapes for Methanol Steam Reforming and the Water Gas Shift Reactions. *Energy Environ. Sci.* **2010**, *3*, 831–837.
- (16) Bruix, A.; Rodríguez, J. A.; Ramírez, P. J.; Senanayake, S. D.; Evans, J.; Park, J. B.; Stacchiola, D.; Liu, P.; Hrbek, J.; Illas, F. A New Type of Strong Metal-Support Interaction and the Production of H₂ through the Transformation of Water on Pt/CeO₂(111) and Pt/CeO₃/TiO₂(110) Catalysts. *J. Am. Chem. Soc.* **2012**, *134*, 8968–8974.
- (17) Barrios, C. E.; Bosco, M. V.; Baltanás, M. A.; Bonivardi, A. L. Hydrogen Production by Methanol Steam Reforming: Catalytic Performance of Supported-Pd on Zinc-Cerium Oxides Nanocomposites. *Appl. Catal., B* **2015**, *179*, 262–275.
- (18) Shido, T.; Iwasawa, Y. Regulation of Reaction Intermediate by Reactant in the Water-Gas Shift Reaction on CeO₂, in Relation to Reactant-Promoted Mechanism. *J. Catal.* **1992**, *136*, 493–503.
- (19) Shido, T.; Iwasawa, Y. Reactant-Promoted Reaction Mechanism for Water-Gas Shift Reaction on Rh-Doped CeO₂. *J. Catal.* **1993**, *141*, 71–81.
- (20) Jacobs, G.; Khalid, S.; Patterson, P. M.; Sparks, D. E.; Davis, B. H. Water-gas Shift Catalysis: Kinetic Isotope Effect Identifies Surface Formates in Rate Limiting Step for Pt/Ceria Catalysts. *Appl. Catal., A* **2004**, *268*, 255–266.
- (21) Meunier, F.; Reid, D.; Goguet, A.; Shekhtman, S.; Hardacre, C.; Burch, R.; Deng, W.; Flytzani-Stephanopoulos, M. Quantitative Analysis of the Reactivity of Formate Species seen by Drifts over a Au/Ce(La)O₂ Water-Gas Shift Catalyst: First Unambiguous Evidence of the Minority Role of Formates as Reaction Intermediates. *J. Catal.* **2007**, *247*, 277–287.
- (22) Burch, R.; Goguet, A.; Meunier, F. C. A Critical Analysis of the Experimental Evidence for and against a Formate Mechanism for High Activity Water-Gas Shift Catalysts. *Appl. Catal., A* **2011**, *409–410*, 3–12.
- (23) Mudiyanse, K.; Senanayake, S. D.; Feria, L.; Kundu, S.; Baber, A. E.; Graciani, J.; Vidal, A. B.; Agnoli, S.; Evans, J.; Chang, R.; et al. Importance of the Metal-Oxide Interface in Catalysis: In Situ Studies of the Water-Gas Shift Reaction by Ambient-Pressure X-ray Photoelectron Spectroscopy. *Angew. Chem., Int. Ed.* **2013**, *52*, 5101–5105.
- (24) Haghofer, A.; Ferri, D.; Föttinger, K.; Rupprechter, G. Who Is Doing the Job? Unraveling the Role of Ga₂O₃ in Methanol Steam Reforming on Pd₂Ga/Ga₂O₃. *ACS Catal.* **2012**, *2*, 2305–2315.
- (25) Takahashi, K.; Takezawa, N.; Kobayashi, H. The Mechanism of Steam Reforming of Methanol over a Copper-Silica Catalyst. *Appl. Catal.* **1982**, *2*, 363–366.
- (26) Jiang, C.; Trimm, D.; Wainwright, M.; Cant, N. Kinetic Study of Steam Reforming of Methanol over Copper-Based Catalysts. *Appl. Catal., A* **1993**, *93*, 245–255.
- (27) Collins, S. E.; Baltanás, M. A.; Bonivardi, A. L. An Infrared Study of the Intermediates of Methanol Synthesis from Carbon Dioxide over Pd/β-Ga₂O₃. *J. Catal.* **2004**, *226*, 410–421.
- (28) Paredes-Nunez, A.; Lorito, D.; Guilhaume, N.; Mirodatos, C.; Schuurman, Y.; Meunier, F. C. Nature and Reactivity of the Surface Species Observed over a Supported Cobalt Catalyst under CO/H₂ Mixtures. *Catal. Today* **2015**, *242*, 178–183.
- (29) Li, C.; Domen, K.; Maruya, K.-I.; Onishi, T. Spectroscopic Identification of Adsorbed Species Derived from Adsorption and Decomposition of Formic Acid, Methanol, and Formaldehyde on Cerium Oxide. *J. Catal.* **1990**, *125*, 445–455.
- (30) Wu, Z.; Li, M.; Mullins, D. R.; Overbury, S. H. Probing the Surface Sites of CeO₂ Nanocrystals with Well-Defined Surface Planes via Methanol Adsorption and Desorption. *ACS Catal.* **2012**, *2*, 2224–2234.
- (31) Mullins, D. R. The Surface Chemistry of Cerium Oxide. *Surf. Sci. Rep.* **2015**, *70*, 42–85.
- (32) Busca, G.; Lorenzelli, V. Infrared Spectroscopic Identification of Species Arising from Reactive Adsorption of Carbon Oxides on Metal Oxide Surfaces. *Mater. Chem.* **1982**, *7*, 89–126.
- (33) Deacon, G.; Phillips, R. Relationships Between the Carbon-Oxygen Stretching Frequencies of Carboxylate Complexes and the Type of Carboxylate Coordination. *Coord. Chem. Rev.* **1980**, *33*, 227–250.

- (34) Senanayake, S. D.; Mullins, D. R. Redox Pathways For HCOOH Decomposition over CeO₂ Surfaces. *J. Phys. Chem. C* **2008**, *112*, 9744–9752.
- (35) Stubenrauch, J.; Brosha, E.; Vohs, J. Reaction of Carboxylic Acids on CeO₂(111) and CeO₂(100). *Catal. Today* **1996**, *28*, 431–441.
- (36) Siokou, A.; Nix, R. M. Interaction of Methanol with Well-Defined Cerium Surfaces: Reflection/Absorption Infrared Spectroscopy, X-Ray Photoelectron Spectroscopy, and Temperature-Programmed Desorption Study. *J. Phys. Chem. B* **1999**, *103*, 6984–6997.
- (37) Gordon, W. O.; Xu, Y.; Mullins, D. R.; Overbury, S. H. Temperature Evolution of Structure and Bonding of Formic Acid and Formate on Fully Oxidized and Highly Reduced CeO₂(111). *Phys. Chem. Chem. Phys.* **2009**, *11*, 11171–11183.
- (38) Rotzinger, F. P.; Kesselman-Truttmann, J. M.; Hug, S. J.; Shklover, V.; Grätzel, M. Structure and Vibrational Spectrum of Formate and Acetate Adsorbed from Aqueous Solution onto the TiO₂ Rutile (110) Surface. *J. Phys. Chem. B* **2004**, *108*, 5004–5017.
- (39) Anisimov, V.; Solovyev, I.; Korotin, M.; Czyżyk, M.; Sawatzky, G. Density-Functional Theory and NiO Photoemission Spectra. *Phys. Rev. B: Condens. Matter Mater. Phys.* **1993**, *48*, 16929–16934.
- (40) Solovyev, I.; Dederichs, P.; Anisimov, V. Corrected Atomic Limit in the Local-Density Approximation and the Electronic Structure of *d* Impurities in Rb. *Phys. Rev. B: Condens. Matter Mater. Phys.* **1994**, *50*, 16861–16871.
- (41) Anisimov, V. I.; Aryasetiawan, F.; Lichtenstein, A. I. First-Principles Calculations of the Electronic Structure and Spectra of Strongly Correlated Systems: the LDA + U Method. *J. Phys.: Condens. Matter* **1997**, *9*, 767–808.
- (42) Ganduglia-Pirovano, M. V.; Hofmann, A.; Sauer, J. Oxygen Vacancies in Transition Metal and Rare Earth Oxides: Current State of Understanding and Remaining Challenges. *Surf. Sci. Rep.* **2007**, *62*, 219–270.
- (43) Da Silva, J.; Ganduglia-Pirovano, M.; Sauer, J.; Bayer, V.; Kresse, G. Hybrid Functionals Applied To Rare-Earth Oxides: the Example of Ceria. *Phys. Rev. B: Condens. Matter Mater. Phys.* **2007**, *75*, 045121.
- (44) Ganduglia-Pirovano, M.; Da Silva, J.; Sauer, J. Density-Functional Calculations of the Structure of Near-Surface Oxygen Vacancies and Electron Localization on CeO₂(111). *Phys. Rev. Lett.* **2009**, *102*, 026101.
- (45) Vayssilov, G. N.; Mihaylov, M.; Petkov, P. S.; Hadjivanov, K. I.; Neyman, K. M. Reassignment of the Vibrational Spectra of Carbonates, Formates, and Related Surface Species on Ceria: A Combined Density Functional and Infrared Spectroscopy Investigation. *J. Phys. Chem. C* **2011**, *115*, 23435–23454.
- (46) Mei, D. First-Principles Characterization of Formate and Carboxyl Adsorption on Stoichiometric CeO₂(111) and CeO₂(110) Surfaces. *J. Energy Chem.* **2013**, *22*, 524–532.
- (47) Finos, G.; Collins, S.; Blanco, G.; del Rio, E.; Cies, J. M.; Bernal, S.; Bonivardi, A. Infrared Spectroscopic Study of Carbon Dioxide Adsorption on the Surface of Cerium-Gallium Mixed Oxides. *Catal. Today* **2012**, *180*, 9–18.
- (48) Vecchietti, J.; Collins, S.; Delgado, J. J.; Malecka, M.; Del Rio, E.; Chen, X.; Bernal, S.; Bonivardi, A. Gold Catalysts Supported on Cerium-Gallium Mixed Oxide For the Carbon Monoxide Oxidation and Water Gas Shift Reaction. *Top. Catal.* **2011**, *54*, 201–209.
- (49) Payne, M.; Teter, M.; Allan, D.; Arias, T.; Joannopoulos, J. Iterative Minimization Techniques for Ab Initio Total-Energy Calculations: Molecular Dynamics and Conjugate Gradients. *Rev. Mod. Phys.* **1992**, *64*, 1045–1097.
- (50) Kresse, G.; Hafner, J. Ab Initio Molecular Dynamics for Liquid Metals. *Phys. Rev. B: Condens. Matter Mater. Phys.* **1993**, *47*, 558–561.
- (51) Kresse, G.; Hafner, J. Ab Initio Molecular-Dynamics Simulation of the Liquid-Metal-Amorphous-Semiconductor Transition in Germanium. *Phys. Rev. B: Condens. Matter Mater. Phys.* **1994**, *49*, 14251–14269.
- (52) Kresse, G.; Furthmüller, J. Efficiency of Ab-Initio Total Energy Calculations for Metals and Semiconductors Using a Plane-Wave Basis Set. *Comput. Mater. Sci.* **1996**, *6*, 15–50.
- (53) Kresse, G.; Furthmüller, J. Efficient Iterative Schemes for Ab Initio Total-Energy Calculations Using a Plane-Wave Basis Set. *Phys. Rev. B: Condens. Matter Mater. Phys.* **1996**, *54*, 11169–11186.
- (54) Kresse, G.; Joubert, D. From Ultrasoft Pseudopotentials to the Projector Augmented-Wave Method. *Phys. Rev. B: Condens. Matter Mater. Phys.* **1999**, *59*, 1758–1775.
- (55) Blöchl, P. E. Projector Augmented-Wave Method. *Phys. Rev. B: Condens. Matter Mater. Phys.* **1994**, *50*, 17953–17979.
- (56) Dudarev, S.; Botton, G.; Savrasov, S.; Humphreys, C.; Sutton, A. Electron-Energy-Loss Spectra and the Structural Stability of Nickel Oxide: An LSDA+U Study. *Phys. Rev. B: Condens. Matter Mater. Phys.* **1998**, *57*, 1505–1509.
- (57) Perdew, J. P.; Burke, K.; Ernzerhof, M. Generalized Gradient Approximation Made Simple. *Phys. Rev. Lett.* **1996**, *77*, 3865–3868.
- (58) Monkhorst, H. J.; Pack, J. D. Special Points for Brillouin-Zone Integrations. *Phys. Rev. B* **1976**, *13*, 5188–5192.
- (59) Rogal, J.; Reuter, K. Ab Initio Atomistic Thermodynamics for Surfaces: A Primer. In *Experiment, Modeling and Simulation of Gas-Surface Interactions for Reactive Flows in Hypersonic Flights*, Papers presented during the AVT-142 RTO AVT/VKI Lecture Series, von Karman Institute, Rhode St. Genèse, Belgium, February 6–10, 2006; Paper 2.
- (60) Fernández-Torre, D.; Carrasco, J.; Ganduglia-Pirovano, M. V.; Pérez, R. Hydrogen Activation, Diffusion, and Clustering on CeO₂(111): A DFT+U Study. *J. Chem. Phys.* **2014**, *141*, 014703.
- (61) Murgida, G. E.; Ganduglia-Pirovano, M. V. Evidence for Subsurface Ordering of Oxygen Vacancies on the Reduced CeO₂(111) Surface Using Density-Functional and Statistical Calculations. *Phys. Rev. Lett.* **2013**, *110*, 246101.
- (62) Badlani, M.; Wachs, I. Methanol: A "Smart" Chemical Probe Molecule. *Catal. Lett.* **2001**, *75*, 137–149.
- (63) Collins, S. E.; Briand, L. E.; Gambaro, L. A.; Baltanás, M. A.; Bonivardi, A. L. Adsorption and Decomposition of Methanol on Gallium Oxide Polymorphs. *J. Phys. Chem. C* **2008**, *112*, 14988–15000.
- (64) Rousseau, S.; Marie, O.; Bazin, P.; Daturi, M.; Verdier, S.; Harlé, V. Investigation of Methanol Oxidation over Au/Catalysts Using Operando IR Spectroscopy: Determination of the Active Sites, Intermediate/Spectator Species, and Reaction Mechanism. *J. Am. Chem. Soc.* **2010**, *132*, 10832–10841.
- (65) Kropp, T.; Paier, J. Reactions of Methanol with Pristine and Defective Ceria (111) Surfaces: A Comparison of Density Functionals. *J. Phys. Chem. C* **2014**, *118*, 23690–23700.
- (66) Binet, C.; Badri, A.; Lavalley, J.-C. A Spectroscopic Characterization of the Reduction of Ceria from Electronic Transitions of Intrinsic Point Defects. *J. Phys. Chem.* **1994**, *98*, 6392–6398.
- (67) Binet, C.; Daturi, M.; Lavalley, J.-C. IR Study of Polycrystalline Ceria Properties in Oxidised and Reduced States. *Catal. Today* **1999**, *50*, 207–225.
- (68) Badri, A.; Binet, C.; Lavalley, J.-C. An FTIR Study of Surface Ceria Hydroxy Groups During a Redox Process with H₂. *J. Chem. Soc., Faraday Trans.* **1996**, *92*, 4669–4673.
- (69) Fernández-Torre, D.; Košmider, K.; Carrasco, J.; Ganduglia-Pirovano, M. V.; Pérez, R. Insight Into the Adsorption of Water on the Clean CeO₂(111) Surface with Van Der Waals and Hybrid Density Functionals. *J. Phys. Chem. C* **2012**, *116*, 13584–13593.